HAL
open science

Continuous maximum flow segmentation method for nanoparticle interaction analysis

Laszlo Marak, Olena Tankyevych, Hugues Talbot

To cite this version:

Laszlo Marak, Olena Tankyevych, Hugues Talbot. Continuous maximum flow segmentation method for nanoparticle interaction analysis. Journal of Microscopy, 2011, 244 (1), pp.59-78. 10.1111/j.1365-2818.2011.03507.x . hal-00865924

HAL Id: hal-00865924

https://hal.science/hal-00865924

Submitted on 25 Sep 2013

HAL is a multi-disciplinary open access archive for the deposit and dissemination of scientific research documents, whether they are published or not. The documents may come from teaching and research institutions in France or abroad, or from public or private research centers.

L'archive ouverte pluridisciplinaire **HAL**, est destinée au dépôt et à la diffusion de documents scientifiques de niveau recherche, publiés ou non, émanant des établissements d'enseignement et de recherche français ou étrangers, des laboratoires publics ou privés.

Continuous maximum flow segmentation method for nano-particle interaction analysis

Laszlo Marak*, Olena Tankyevych and Hugues Talbot

Université Paris-Est, Département d'Informatique Gaspard-Monge,

Équipe A3SI, ESIEE Paris, Cité Descartes, BP 99, F-93162 Noisy-le-Grand Cedex, France

{ujoimro, tankyevych}@gmail.com, talboth@esiee.fr

January 26, 2011

Abstract

In recent years, tomographic 3D reconstruction approaches using Electrons rather than X-Rays have become popular. Such images produced with a Transmission Electron Microscope (TEM) make it possible to image nanometer-scale materials in 3D. However, they are also noisy, limited in contrast, and

*PGP: A812 3708 B2E1 3B42 500E D50C 49A0 88FA C060 3F65

most often have a very poor resolution along the axis of the electron beam. The analysis of images stemming from such modalities, whether fully or semi automated, is therefore more complicated. In particular, segmentation of objects is difficult. In this article, we propose to use the continuous maximum flow segmentation method based on a globally optimal minimal surface model. The use of this fully automated segmentation and filtering procedure is illustrated on two different nano-particle samples and provide comparisons with other classical segmentation methods. The main objectives are the measurement of the attraction rate of polystyrene beads to silica nano-particle (for the first sample) and interaction of silica nano-particles with large unilamellar liposomes (for the second sample). We also illustrate how precise measurements such as contact angles can be performed.

Keywords: electron tomography; image analysis; continuous optimization ; Hough circles; transmission electron microscopy.

1 Introduction

In this paper, we study the application of image analysis to nano-tomography images and we present an image segmentation technique for this purpose. Image segmentation is the task of decomposing an image into a set of disjoint components that are each semantically consistent within themselves (e.g.

finding the red blood cells in histology samples, or people in a photograph). It is an essential task for further image-based studies since it enables measurements to be made on objects, which otherwise would be indistinguishable collections of pixels. Segmentation is one of the fundamental tasks of computer vision, and there exist no generic method to achieve it. In the rest of the paper, we will perform segmentation by finding good-quality contours (in 2D) or surfaces (in 3D) around objects of interests.

Here, we focus on the automated segmentation and interaction measurements of nano-particles in electron tomography. While there exists a number of papers that have already applied image analysis to nano-particle studies (Fisker et al., 2000, Woehrle et al., 2006), segmentation of such particles can be especially difficult, for reasons outlined below.

Motivation

Nanometer-scale particles possess singular physical and chemical properties due to their dimensions, which have motivated a rapidly growing interest in recent years (Fendler, 1998, Schmid, 2004). These new-found properties have led to the novel applications of these nanomaterials to many areas, such as catalysts, semiconductors, sensors, drug carriers, and personal care products (Chan, 2006, Rosi & Mirkin, 2005, Valden et al., 1998). Commercial

products including engineered nano-materials in their make-up are expected to become more frequent in the near future. As a consequence, both consumer and professional exposures to these materials are likely to increase in proportion to their use in the society. However, these nanomaterials can be potentially harmful to human and environment due to the large percentage of atoms lying on their surface and unusually high reactivity (Nel et al., 2006).

It is therefore important to study nano-materials both at the chemical and physical level. For this, Transmission Electron Microscopy (TEM) is the method of choice for nano-particle samples (Le Bihan et al., 2009). However, while standard TEM can provide sufficient two-dimensional resolution, it has insufficient depth sensitivity to detect internal three-dimensional structure. The main limitation is that it is a 2D projection of a 3D object. The technique does detect internal 3D structures, but as a 2D projection. To palliate this problem, electron tomography, initially proposed by W. Hoppe in the 1970's Hoppe (1974), has become increasingly popular (Downing et al., 2007) in order to obtain 3D views of nano-scale materials. Electron tomography works broadly on the same principles as X-ray tomography, but uses electrons instead. Also, instead of a dedicated instrument, standard TEM equipment with relatively minor add-on can be used to acquire the data. The sample under study is placed in an automated stage control, which tilts at regularly spaced angles and the microscope digitally acquires a projected image. To-

mography software is then used to perform a 3D reconstruction from these projections. Due to limitations in the achievable tilt angle, the resolution of the images that are obtained is usually very poor along the electron beam axis, and can also be noisy and feature low contrast. We recommend (Midgley et al., 2007) for further reading.

In this work, we are interested in assessing two different nano-article interaction studies with image analysis techniques. For the first one, the objective is to get an insight into the surface contact of polystyrene beads with silica nano-particles extracted from tomographic reconstructions. One slice of a sample can be seen in Fig. 1 [1]. The interest of the segmentation lies in the measurement of the attraction rate of the beads to the nano-particle. The attraction is measured by the contact angle.

For the other sample, we focus on interaction of silica nano-particles with large unilamellar liposomes (see Fig. 2 for an image slice example) [2].

Automated image analysis

Once the image is obtained, the next step is often to analyse the content through for instance particle counting, size measurements, composition and interaction studies. While a manual analysis of nano-tomography data is of

[1] The material and the problem is described in more detail in Taveau et al. (2008).

[2] More details on the material for this application can be found in Le Bihan et al. (2009).

course possible (Nickell et al., 2005), it is often not desirable. One reason is that the data is inherently 3D, which is difficult to represent on paper or on computer screen, and difficult to interact with. Although 3D viewing software packages have made enormous progress, interactive segmentation (i.e. finding the contour or the enclosing surface) of objects can still take months. Typically, practitioners endeavor to detour objects in 2D interactively slice by slice, or they try to set a global threshold in order to find a suitable grey-level iso-surface. Specifying surface elements manually is generally infeasible. Specifying contours slice-by-slice is technically possible when contours are easily visible, but even then can lead to inconsistent topology (Kang et al., 2004). It is also very difficult when contour information is not reliable, as is the case in nano-tomography. When noise is present in high levels, finding a suitable iso-surface by thresholding can prove challenging and time-consuming. There is also a potential for human error due to fatigue, perception bias and operator variations. These effects have been well-documented in 2D studies and also in 3D in the context of medical imaging, which is similar in many respects (Martin et al., 2001, Senan et al., 1999). Therefore, there is a need for methods that are able to find the contour of objects reliably, even in the presence of high levels of noise.

On the other hand, while human operators find it typically difficult to detour objects in 2D or 3D, they are usually able to identify objects reliably

and so are able to guide segmentation through interaction. It is therefore important to provide a segmentation method which allows operators to interact easily with the results obtained (Grady, 2010).

The need for a specific segmentation method

Often sufficiently precise contours are necessary for accurate segmentation of image data. For this, we need the following conditions to be satisfied by a segmentation method: 1) have objective optimization criteria; 2) feature few arbitrary parameters; 3) be little sensitive to noise; 4) be able to optionally interpolate missing data due to the missing wedge effect; 5) allow interactivity; and 6) feature as few inherent artifacts as possible.

Since the late 1980s, optimization methods have been used to address a wide variety of problems in computer vision, including segmentation. Early optimization approaches were formulated in terms of active contours and surfaces (Kass et al., 1988a) and then later level sets (Sethian, 1999b). These formulations were used to optimize energies of varied sophistication (e.g., using regional, texture, motion or contour terms (Paragios, 2000)) but generally converged to a local minimum, generating results that were sensitive to initial conditions and noise levels. Consequently, more recent focus has been on energy formulations (and optimization algorithms) for which a global

optimum can be found.

The max-flow/min-cut problem on a graph is a classical problem in graph theory, for which the earliest solution algorithm goes back to Ford and Fulkerson (Ford & Fulkerson, 1956). Initial methods for global optimization of the boundary length of a region formulated the energy on a graph and relied on max-flow/min-cut methods for solution (Boykov & Jolly, 2001, Kolmogorov & Zabin, 2004). It was soon realized that these methods introduced a so-called grid bias (also called metrication error) for which various solutions were proposed. One solution involved the use of a highly connected lattice with a specialty edge weighting (Boykov & Kolmogorov, 2003a), but the large number of graph edges required to implement this solution could cause memory concerns when implemented for large 2D or 3D images.

To avoid the gridding bias without increasing memory usage, one trend in recent years has been to pursue spatially *continuous* formulations of the segmentation problem (Appleton & Talbot, 2006, Chambolle, 2004, Nikolova et al., 2006). Historically, a continuous max-flow (and dual min-cut problem) was formulated by Strang (Strang, 1983b). Strang's continuous formulation provided an example of a *continuization* (as opposed to *discretization*) of a classically discrete problem, but was not associated to any algorithm. Work by Appleton and Talbot (Appleton & Talbot, 2006) provided the first PDE-

based[3] algorithm to find Strang's continuous max-flows and therefore optimal min-cuts.

This method, named in the remainder Continuous Maximum Flows (CMF) is essentially a convex reformulation of the classical Geodesic Active Contour (GAC) framework (Caselles et al., 1997a), which is widely used in 3D image segmentation. Being convex means, that the PDE can be solved by the broken-line algorithm and it provides a globally optimal solution with no metrication artifact. It is not a limitation on the form of the object which can be non-convex or non smooth. In addition, the method is efficient in 3D, and is therefore a good candidate for our purpose.

In the present work, we are applying the CMF method and both pre-, and post-processing image analysis methods to two different nano-material problems.

2 Electron nano-tomography

Electron nano-tomography originally proposed in the 1970s that uses a Transmission Electron Microscope (TEM) as an illuminating source for 3D object tomography, but has lately become more popular due to the increased avail-

[3]PDE–Partial Differential Equation, are a type of differential equation, i.e., a relation involving an unknown function of several independent variables and their partial derivatives. Partial differential equations are used to formulate, and thus aid the solution of, problems involving functions of several variables.

ability of effective reconstruction software.

Principles

While more standard tomography techniques use X-Rays as source, nano-tomography uses electrons instead. The main benefit of using electrons is the significant increase in resolution compared to X-Rays. As electrons in TEM behave in some ways as waves with a very high frequency, they allow for nanometer scale resolution, while X-Ray sources are typically limited to about micrometer scales resolution.

The general principles of electron nano-tomography (ET) are broadly similar to standard X-ray tomography (Kak & Slaney, 1999), in the sense that projection images around the volume of interest are used, and the reconstruction of a 3D image of this volume is effected through the use of inverse tomography algorithms (for instance filtered back-projections, iterative methods, etc). Electrons traverse the material to be imaged, and are either left untouched, absorbed, diffracted or deflected as a result. The projection of the intensities as recorded by the TEM's imaging device is, under suitable conditions, comparable to an attenuation image, although many artifacts are typically present.

The sample, rather than the device, is rotated along one (or sometimes

two axes), and projection images are recorded at regular angles. See Fig. 3 for simplified schematics. Similarly with CT scan, the angle(s) of tilt can be automatically associated with all recorded projection.

Features and limitations of the technique

One feature of TEM is that since electrons are negatively charged fermions, they readily interact with matter and are easily scattered by positively charged atom nuclei. As a result, unlike X-Rays, electrons cannot penetrate much into matter, and are affected by sample chemical contents: heavy atoms deviate electrons more than lighter ones. As a result, this so-called chemical (or Z-number) contrast is present in addition to absorption contrast. This effect can be used productively in Z-number contrast tomography Midgley et al. (2007). The loss of energy in exiting electrons resulting from this interaction can also be used to derive chemical content in other modalities such as EFTEM Möebus & Inkson (2003).

However , due to this interaction with matter, preparation for TEM imaging implies thinning the sample under study as much as possible, so as to make it mostly transparent to electrons, using physical processes such as ion mills for instance. For some materials and high resolution needs, the final sample may be only a few hundreds of nanometer thick at its thinnest point.

Because the final sample is then extremely fragile, it is currently impossible to obtain such thinness over a large area, and much less in such a way that the final sample is thin in two directions at once (like a thread or a needle). In other words, the final sample is most often like a thin layer in a relatively deep well, as illustrated in Fig. 4. Even in naturally flat, thin samples, such as nanoparticles dispersed on a carbon grid, the grid holding the sample induces shadowing at high angles.

As a direct consequence, the sample cannot be illuminated in all directions around it, unlike a patient in a CT scanner. This means that the electron beam cannot illuminate the sample in directions that are too far away from the normal to the thin layer. Finally, in a typical ET scanner the specimen holder sits inside the objective lens pole piece so there is very limited space for tilting, even if the sample would be string-like. Typically, illumination much beyond 70° from the normal is difficult or impossible, and a complete set of projections cannot be obtained, from which to derive a complete tomographic reconstruction. To ameliorate the situation somewhat, tilt sequences can be recorded along several angles, but *in fine* there is most often a so-called "missing wedge" in the projection space.

In practice, this translates into 3D images that exhibit noise and weak or elongated edges in the direction of the normal to the surface of the sample (i.e. the direction of the beam when the sample is untitled), but relatively

strong features in the perpendicular directions to this normal. Fig. 5 shows some of these effects. This is an image of a polystyrene ball. Along the "equator" of the ball, edges are strong, but at the "poles", edges are weak.

Image analysis challenges

Segmentation of nanotomography images is difficult because of these characteristics, as we illustrate on Fig. 6. In particular, because of the missing wedge and strong noise, thresholding is unreliable (see Fig. 6(a)). For the same reasons, watershed Beucher & Lantuéjoul (1979), Meyer & Beucher (1990) is prone to leaking (see Fig. 6(b)). More recent methods, such as graph cuts Boykov & Jolly (2001), Boykov & Kolmogorov (2003b) are more successful but due to their anisotropic formulation, they tend to find edges that are aligned with the principal directions of the image sampling grid (see Fig. 6(c)), leading to clipped results. Here, the need for a segmentation solution which is little sensitive to noise, globally optimal and isotropic is essential. In the following section, we describe an improved solution.

3 Continuous maximum flows and minimal surfaces

In this section, we describe the continuous maximum flows model used for the segmentation of particles of nano-tomography images. We assume sufficient regularity for all functionals whose practice is usually met in physical systems.

As a fundamental idea, let g be a function on $\Omega \subset \mathbb{C}(\mathbb{R}^n)$ that defines a local metric cost, i.e. the value of g at point x is the cost of traversing point x. We will assume that g is scalar and provides values in $\mathbb{R}$, and we will call this function our *cost function*. Furthermore, let S (*source*) and P (*sink*) be two disjoint subsets of Ω. Let all closed simple hyper-surfaces[4] s with finite area (not necessarily connected) be those that do contain the source and do not contain the sink. In some sense, we can define the source of the segmentation as a marker for the interior of the object to be segmented, and the sink as a marker for its exterior.

Then we can define the following functional:

$$E(s) = \oint_s g ds, \tag{1}$$

called the total weight or total cost of s. As $E(s) \leq \text{area}(s) \cdot \max(g)$ is

[4] A simple hyper-surface is a curve in 2D or a surface in 3D that does not intersect itself.

finite for bounded g. Furthermore, there exists at least one hyper-surface M exhibiting minimum weight (Strang, 1983a). In a discrete domain this minimum surface can be computed using the Ford and Fulkerson maximum flow graph algorithm (Ford & Fulkerson, 1962), which was improved in the digital image context by Boykov & Kolmogorov (2003b).

In the continuous domain, M can be computed directly for every cost function g and sets P, T using for example active contours or surfaces methods (Kass et al., 1988b), or level-sets methods (Caselles et al., 1997b, Sethian, 1999a). However, these methods compute surfaces iteratively via gradient descent schemes, and thus the solution is only locally optimal. Hence, the solution depends on initialization and noise levels. On the other hand, the algorithm presented by Appleton & Talbot (2006) provides a globally optimal solution to this problem. The solution is obtained in form of a smooth quasi-binary function[5] monotonically decreasing from source to sink. The iso-surfaces of this function will represent the minimum surface. As with the continuous nature of the algorithm, in some cases, it provides a sub-pixel accurate positioning of the minimal surface.

The differential geometric approach, that is to say, segmentation by optimization (Eq.1) is advantageous in cases where only parts of the contour are known. These are parts of the image where g is close to a constant. In this

[5]One for which most values are either 0 or 1.

case, this approach interpolates the known area with patches of minimum surfaces (in the geometric sense).

The solution with the maximum flows method depends on choices of: 1) a relevant cost-function g to our problem; 2) sources and 3) sinks. Examples of syntethic objects can be found on Fig. 7.

3.1 The choice of the image function

In the current framework, we are seeking the optimal curve (the one that has the optimal integral) around the source of an object. However, on point-wise sources $E(s) = \oint_s \mathrm{d}G = \oint_s g\mathrm{d}x \leq \mathrm{surf}(s) \cdot \max_s g \to 0$ if we take smaller and smaller surfaces around S. So, that if we take a small surface around S, it will have small cost, but not on the contour of the object, like in Fig. 8. This can be overcome in two ways. The first possibility is that impose S to have some minimum length or surface. The boundary ∂S will then have non-zero cost, so that we can find the contours if they are smaller than the cost of the boundary. The second possibility is to modify our cost function with a particular weighting. For example, in a constant image L, lets define g as:

$$g_I(P) := \frac{1}{\mathrm{d}(P, S) \cdot (1 + \nabla L)} \tag{2}$$

Here, $d(A, B)$ denotes the distance of A and B.

Now let us look at the circles with ray r around the point-wise S:

$$\oint_{|\overline{\mathbf{x}}|=r} g_I(\overline{\mathbf{x}})\ \mathrm{d}\overline{\mathbf{x}} = \oint_0^{2\pi} \frac{r}{\underbrace{\mathrm{d}\left(\begin{bmatrix} r\sin(t) \\ r\cos(t) \end{bmatrix}, S\right)}_{r} \cdot (1+\nabla L)}\ \mathrm{d}t = \oint_0^{2\pi} \frac{\mathrm{d}t}{1+\nabla L} \tag{3}$$

If L is constant then Eq.3 gives 2π for all the circles around S. It can also be proven that these circles are the minimum cost curves of this measure. If ∇I is different from 0 at some point A (For example there is one point in I), then the "cheapest" curve will be the circle that contains A.

The following, complementary way to look at the problem is also true: if an image I is constant between the parts of the contour, then on these parts the solution will be interpolated with a circle. This approach is used in section 4.2.

We can extend this idea and define any set of curves D which do not intersect. It can be proven that there exists a weighting W, where the minimum cost curves are those of D.

This approach will tend to put the surface near the high frequency places before the curves of D. So it has a limited usage if the noise is at the level of the contours, like in Section 4.2, Fig. 9. Also there are cases where the set of curves is more difficult to define, like in section 4.3, Fig. 10.

The remaining challenges are how to choose sources and sinks. In the next few sections we present the ways we have solved this in the cases of weak gradient or/and high noise.

3.1.1 Calculation of the cost function

A relatively easy way to attract a minimal surface near object contours is to consider the following cost function, given by $g = \frac{1}{1+\|\nabla I\|}$. This cost function is high in relatively constant parts of the image, but drops to zero near edges, which are areas of high gradient. However, in regions where g is near-constant (in our images, this will occur near the extremities of objects under study that are along the electron beam, i.e. near the "poles" of objects), the minimum surface is a portion of plane. This means that the minimum surfaces will be attracted by the global noise. In this case the key observation is that the reconstruction-created noise shows parallelism with the axes. The result of this initial segmentation is close to a truncated sphere. To correct this defect, we used a *modified* g. More precisely, we used separable spline-interpolated gradient (available in (Foundation, 2010)) in direction from the source to the point and the sphere weighting introduced in Section 3.1.

The formal definition follows:

For a one-dimensional vector $\overline{\mathbf{x}}$, its continuous spline interpolation is denoted with $f_{\overline{\mathbf{x}}}$. For a 3D image I, the three axial vectors that contain the

point P are denoted with $\overline{\mathbf{x}}_P$, $\overline{\mathbf{y}}_P$ and $\overline{\mathbf{z}}_P$, respectively. The gradient of the image I in point P is defined by $\nabla I_P = \begin{pmatrix} \partial f_{\overline{\mathbf{x}}_P} \\ \partial f_{\overline{\mathbf{y}}_P} \\ \partial f_{\overline{\mathbf{z}}_P} \end{pmatrix}$.

To calculate the directional gradient in point P we use the direction vector $\overline{\mathbf{c}} := \overline{\mathrm{CP}}$. The final cost function used in this case is

$$g(P) = \frac{1}{\underbrace{\mathrm{d}^2(P,S)}_{*} \cdot (1 + \underbrace{\overline{\mathbf{c}} \cdot \nabla I}_{**})} \tag{4}$$

Here, (**) is the gradient in direction of $\overline{\mathbf{c}}$ and (*) is the square of the distance from the source. The square exponent is needed because the area of the minimum surface is proportional to the square of the radius of the object. This cost function filters the artifacts in the direction z and the closer we are to the direction, the more we ignore the noise. An example of an image of a polystyrene ball segmented by the CMF method is shown in Fig. 9(a). Fig. 9(b) shows the ball segmented without the cost function weighting. We can observe an incorrect reconstruction due to weak gradient in this area of the image. In Fig. 9(c), 9(d) a better segmentation results are shown. It was achieved using the $\frac{1}{r}$ weighting described above.

3.1.2 Curvature estimation

Curvature estimations were provided in some key areas of the image, for instance near points of contact between nanoparticles and liposomes as well as in the case of the membrane of the liposome. In the presence of a reliable surface segmentation and in the continuous domain, the local curvature is well-defined mathematically and can be estimated using local second derivatives. Curvature estimation is also possible from implicit surface representations (Goldman, 2005). However, in our case we found that the precision of these methods was not good enough due to discretization and noise. A scale must be chosen at which to estimate the curvature and appropriate smoothing must be applied with some caution, in particular in order to preserve topology.

Instead, we developed semi-local representations of curvature appropriate to our problem, in particular given our priority regarding topology preservation. We started from the medial axis representation of our segmented result S (Blum, 1961) and found the extremities of this representation. The medial axis is the locus of the centers of maximal disks (2D) or balls (3D) included in S. Maximal balls are such that no ball can strictly contain them and still be included in S. Their center lie at local centers of symmetry for S, and they touch (and are in fact tangent to) the border of S on at least

two distinct points. The superset of the medial axis that is connected and topologically equivalent to S is called the skeleton of S, and there exists efficient algorithms for computing the medial axis and the skeleton in 3D, see for instance (Lobregt et al., 1980, Zrour & Couprie, 2005). Skeleton extremities can be detected using local configurations (e.g. points with a pre-determined number of connected neighbors).

3.2 Source and sink determination

One of the keys to maximum flow segmentation is the choice of the source. In the model we assume three things: the source is inside the object, the sink is outside of it and we segment only one object at a time. While there exists situations where the choice of the source can be arbitrary placed within the object, in many cases, however, the segmentation can be improved with a good choice of source. While segmenting more objects at a time is theoretically possible, the topology of the final object is not guaranteed. There exist examples where more isolated sources still lead to a single object after the segmentation.

In our case, due to the missing wedge effect, a more precise choice of source and sink can considerably improve the segmentation results. In Section 4.2 we have used a preprocessing technique to determine the "centres" of the

objects. From these carefully chosen sources we could apply a position-based noise filtering on the cost function g which led to our final segmentation.

In general, sinks are made of 3D bounding boxes around known objects of interest and do not present a strong challenge. In other cases, they might be derived from previous segmentations.

3.3 Calculation of the optimal surface

The continuous maximum flow system is described by the following system of equations:

$$\frac{\partial P}{\partial \tau} = -\nabla \cdot \overline{\mathbf{F}} \tag{5}$$

$$\frac{\partial \overline{\mathbf{F}}}{\partial \tau} = -\nabla P \tag{6}$$

$$|\overline{\mathbf{F}}| \leq g \tag{7}$$

Here P represents a scalar (pressure-like) field and F a flow vector field (a speed-like field). P is forced to 1 on the source and 0 on the sink. The equation can be solved numerically (by simulation). Assuming convergence

for a given g, the steady-state solution is:

$$\nabla \cdot \overline{\mathbf{F}} = 0 \tag{8}$$

$$\nabla P = 0 \qquad \text{if} \quad |\overline{\mathbf{F}}| < g \tag{9}$$

$$\nabla P = -\lambda \overline{\mathbf{F}} \qquad \text{if} \quad |\overline{\mathbf{F}}| = g \tag{10}$$

The Eq. 8 simply restates the conservation of the flow. Eq. 9 applies if the flow has stabilized during the evolution without the constraint (Eq. 7). At stability, direction or magnitude of the flow vector field cannot change. From Eq. 6,7 we can deduce that $\nabla P \cdot \overline{\mathbf{F}} \leq 0$, which means that P is a monotonically decreasing function along the flow lines. If $\overline{\mathbf{F}}$ is dense, as it is divergence-free, these flow lines can only initiate in the source and end at the sink.

Now, we define set $A = \{x | P(x) > p\}$ with $0 < p < 1$. On the iso-surface $Y := \partial A$ the $\nabla P \neq 0$ by construction, which means, that in these points (Eq.7) applies thus:

$$\int_A \nabla \cdot \overline{F_Y} = \oint_Y \overline{N_Y} \cdot \overline{\mathbf{F}} \mathrm{d}Y = \oint_Y g \mathrm{d}Y = \oint_Y \mathrm{d}G \tag{11}$$

This implies, that every iso-surface of P is a minimal surface. If there is only one minimum, this also means that the P field can be $0 \leq P \leq 1$ only on a

zero measure set.

Computation of minimal surfaces by this flow simulation is reasonably fast. For instance, in the case of section 4.2, steady-state convergence of a 116x116x116 pixel image is reached in 2000 iterations in 80 seconds on a dual-core AMD 2.5GHz Opteron CPU. Memory consumption is in the order of 4 times the initial image size in single-precision floating point format.

4 Segmentation and interaction analysis of nanoparticles

4.1 Image acquisition

The volume images are reconstructed from a series of projected 2D images. The object is turned around its axe and full 2D attenuation pattern is recorded at each angle. In this application, a 5 μl sample was deposited onto a holey carbon coated copper grid, while the excess was blotted with a filter paper. The grid was plunged into liquid ethane, cooled with liquid nitrogen (Leica EM CPC). Specimens were maintained at a temperature of approximately -170 °C, using a cryo holder (Gatan). For the acquisition, the images were observed with a FEI Tecnai F20 electron microscope operating at 200 kV and at a nominal magnification of 50 000× under low-dose conditions. Im-

ages were recorded with a 2000×2000 slow scan CCD camera (Gatan). For cryo-electron tomography, tilt-series were collected automatically on both FEI Tecnai F20 and Tecnai G2 Polara from $-60°$ to $+60°$ with $2°$ angular increment using the FEI tomography software. Images were recorded on CCD camera at a defocus level between -8 μm and -4 μm. The pixel size at the specimen level varied between 0.5 nm and 0.36 nm. The sample was injected with high intensity particles before the recording, so the exact position of the carbon grid could been determined. For image processing, colloidal gold particles were used as fiducial markers. The 2D projection images were then binned by a factor of two and aligned with the IMOD software (Mastronarde, 1997). Finally the tomographic reconstructions were calculated by weighted back-projection using Priism/IVE package (Chen et al., 1996).

Orientation particles can be seen as white spots in Fig. 11. However, as the carbon grid can only be turned around within about 120 degrees (due to the thickness of the grid), there are some parts of the object which are not present in the volume image. The result of the microscopy are three-dimensional images, however the signal-to-noise ratio becomes very low near object's poles due to missing wedge effect. An example can be observed in Fig. 5.

In this situation, it is desirable to present both the reliable segmentation, i.e. the part of the contour that was detected based on strong edge infor-

mation, and the interpolated ones. In the following, we are detailing the filtering and the segmentation procedure with the described algorithm of the maximum flows and its optimization applied for two types of samples.

4.2 Polystyrene beads nucleated around silica nanoparticles

The material consists of polystyrene nodules and silica bead embedded in a substrate. These roughly spherical objects of size range 100-300 nm are nucleated around an existing silica bead. One slice of a sample can be seen in Fig. 1. The work by Taveau et al. (2008) details all materials and methods.

The aim is to get an insight into the surface contact of polystyrene beads with silica nano-particles extracted from tomographic reconstructions. For this, the particles are automatically segmented and then their contact angles are also automaticlaly measured.

In order to prove the uselfulness of the max-flow method, we compare its performance to other widely used segmentation algorithms: simple threshold, watershed algorithm and the combinatorial graph cuts (that is the Ford-Fulkerson maximum flow algorithm). In the test images, we first applied a median filter, then we segmented the same filtered image by all the comparison algorithms and CMF. The final segmentation results are superimposed on

the original image. This example shows the side-effects of these segmentation algorithms.

The Ford-Fulkerson, graph-cut and watershed may perform similarly on 2D images, whereas they have radically different performances when the problem becomes 3D on this data. The results of these four different methods can be seen in Fig. 6. In this case, the simple threshold of the image cannot produce any usable propositions Fig. 6 (d). We can see that the Ford-Fulkerson algorithm will converge on flat limiting planes instead of spherical ones and that watershed cannot find the limits of the objects at all, making thus the object reach the borders of the image. Considering these examples, the continuous maxflow algorithm equipped with the specialized gradient described earlier can be a good alternative over these methods. It can interpolate the missing (or weak) parts of the gradient with a simple form; in this case close to a sphere, but concave objects would also be possible. More complex objects, like facets of a crystal have not yet been tried, but would be an interesting problem to look at.

In order to segment the image with the maximum flows method from section 3, it is desirable to filter out the noise. As well, we need to specify a *source* and a *sink*.

As a preprocessing step, in order to reduce the noise in the original data (see Fig. 1) we used several filtering steps. 3D median filter was used in order

to reduce speckle and salt-and-pepper noise. 2D edge extraction with the first derivative on a large scale in order to smooth out the noise. Afterwards, a 3D connectivity filter was used in order to eliminate smaller connected areas after thresholding Breen & Jones (1996). A series of morphological openings and closings were useful in reconnecting and reconstructing the 2D circles. These filtering results can be observed in Fig. 12 .

Due to the missing wedge effect, on some slices, insufficiently reconstructed bead poles appear very dim, while well-reconstructed bead slices near the equator appear well separated from the background as in Fig. 5.

For this sample, in order to compensate for this drawback, we have used a preprocessing technique to determine the centres of the particles as closely as possible. The complete bead surface is interpolated by segmentation of its circles from the fully reconstructed (horizontal) image slices. The bead surfaces are used as *sources* for the maximum flow method segmentation.

In order to detect circles from 2D slices of the image volume, the Hough circle transform was used. The original Hough transform (Hough, 1962) and its derivatives have been largely applied and recognized as a robust technique (Illingworth & Kittler, 1988) even in the presence of heavy noise. The circle Hough method did indeed succeed in localizing circle centres and radii even from incomplete initial circles (see Fig. 13).

Once the centres have been determined, these centres were used as sink for

the maximum flow method. We have considered one bead at a time. In this case the extent of the beads is predictable. To facilitate our task without the loss of generality we could assume that a bead is fully contained within $0.7R$ to $1.2R$, where R is the estimated radius of the bead[6]. For the segmentation of each bead, as a *source* marker, a sphere with radius $0.7R$ centered in C was used. The complement of a sphere with radius $1.2R$ centered in C was used as the *sink* marker. This step accelerated the speed of the segmentation as the region excluded was omitted during the segmentation.

Due to the gradient's high sensitivity to noise, we used the gradient of a cubic spline (Foundation, 2010) with some improvements: First the gradient is calculated on each line in each direction with an approximating spline. A spline is a function defined in our case on a line. At each integer point the value of the spline is the same as the image intensity and its derivatives up to degree 3 can be computed analytically.

Here the key observation was, that the noise is roughly parallel to the axes. We could therefore filter the noise from the gradient by calculating a **directional** gradient from the centre. This is done as follows: for a point A to which we would like to know the value of the directional gradient, we consider the ray[7] $\overline{\mathbf{OA}}$, where O is the centre of the bead. At point A we

[6] the estimated radius is a byproduct of the Hough transform
[7] half-line

calculate the sum of the scalar products of the gradients in each direction $g_d = \overline{OA} \cdot \overline{g_x} + \overline{OA} \cdot \overline{g_y} + \overline{OA} \cdot \overline{g_z}$. The higher degree is used to avoid local fluctuations caused by the noise. Finally, the segmentation was performed using the continuous maximum flows method and the results can be observed in Fig. 14.

4.2.1 Contact angle measurement

The interest of the segmentation lies in the measurement of the attraction rate of the beads to the nanoparticle. The attraction is measured by the contact angle.

The common way of the angle calculation is Axisymmetric Drop Shape Analysis (Cheng et al., 1990). In this method a model of the bead is fitted to the image while minimizing the quadratic difference from the image. This way accurate angle measurements can be performed.

However, this method supposes that the physical model of the bead is known and precise. In our case, we do not make any assumptions about the physical properties of the material, so we perform direct angle measurements. In our case, the image plane is projected to the $\overline{\mathbf{x}}\ \overline{\mathbf{y}}$ plane using an angle-preserving conformal map. Secondly, we find the contact point, and finally, we interpolate the contact arcs with a circle calculating the angle between the upper and lower interpolating circles.

Projection of the image We consider the two center points of the beads A and B. We want to consider the planes containing the line $\overline{\mathbf{AB}}$. For the rotation, we use $\overline{\mathbf{x}}$ as the reference vector and $\overline{\mathbf{AB}} \times \overline{\mathbf{x}}$ as the third vector of the base. The basis $\underline{\underline{\mathbf{B}}}_1 = \left[\overline{\mathbf{x}}, \overline{\mathbf{x}} \times \overline{\mathbf{AB}}, \overline{\mathbf{AB}}\right]$ will be our reference basis.

As we want to calculate the angle for every possible cut, we rotate the basis B_1 around the axis $\overline{\mathbf{AB}}$. For this, we project the basis into the origo ($\underline{\underline{\mathbf{O}}}$) and then we apply the rotation transformation. Formally:

$$\underline{\underline{\mathbf{R}}} = \begin{bmatrix} \cos\alpha & -\sin\alpha & 0 & 0 \\ \sin\alpha & \cos\alpha & 0 & 0 \\ 0 & 0 & 1 & 0 \\ 0 & 0 & 0 & 1 \end{bmatrix}$$

will be the rotation transformation and

$$\underline{\underline{\mathbf{O}}} = \begin{bmatrix} 1 & 0 & 0 & 0 \\ 0 & 1 & 0 & 0 \\ 0 & 0 & 1 & 0 \\ 1 & 1 & 1 & 1 \end{bmatrix}$$

will represent the origin basis. $\underline{\underline{\mathbf{T}}} = \underline{\underline{\mathbf{R}}} \cdot \underline{\underline{\mathbf{O}}}^{-1}$ will project the reference basis to the origo, with $\overline{\mathbf{z}}$ matching $\overline{\mathbf{AB}}$. From this $\underline{\underline{\mathbf{B}}}_2 = \left(\underline{\underline{\mathbf{T}}}^{-1} \cdot \underline{\underline{\mathbf{R}}} \cdot \underline{\underline{\mathbf{T}}}\right) \cdot \underline{\underline{\mathbf{B}}}_1$ will represent the projection basis which is the reference basis $\underline{\underline{\mathbf{B}}}_1$ rotated with

angle α. For the angle measurement, we want to project the axe $\overline{\mathbf{AB}}$ to the axe $\overline{\mathbf{y}}$, so we swap the third and the second column of $\underline{\underline{\mathbf{B}}}_2$. We will mark this with $\underline{\underline{\mathbf{B}}}_2^{'}$. In the last step we calculate the projection matrix

$$\underline{\underline{\mathbf{PR}}} = \underline{\underline{\mathbf{B}}}_2^{'} \cdot \underline{\underline{\mathbf{O}}}^{-1}$$

The $\underline{\underline{\mathbf{PR}}}$ matrix will project the points of the $\overline{\mathbf{x}}\ \overline{\mathbf{y}}$ plane to the plane around the axe $\overline{\mathbf{AB}}$. From this we calculate the actual intensity by nearest neighbour interpolation.

Isolation and interpolation of the contact arcs As shown in Fig. 15, we can now conformingly map the cutting planes to 2D images. The neck of the object can be found by a simple pass on the image looking for the closest point to the axis.

For the angle interpolation, we consider the radius r from the bottle neck point and we separate the upper and the lower arcs. The circles, which minimize the square error will represent the interpolation of the derivatives of the images.

Finding the best fitting circle For the best circle fit we use a modified version of the ellipse fitting algorithm from Fitzgibbon et al. (1999). The description of the algorithm follows:

Let's assume, that our circle is defined by the equation:

$$a\left(x^2+y^2\right)+bx+cy+d=0, \tag{12}$$

where $\overline{\mathbf{a}}=\{a,b,c,d\}^T$ and $\overline{\mathbf{x}}=\{x^2+y^2,x,y,1\}^T$.

To find the fitting circle, we minimize the algebraic distance:

$$\mathrm{dist}(\overline{\mathbf{a}})=\sum_{i=1}^{N}\left(\overline{\mathbf{a}}^T\cdot\overline{\mathbf{x}}\right)^2 \tag{13}$$

If we reformulate Eq. 12 to the conventional form:

$$\left(x+\frac{b}{2a}\right)^2+\left(y+\frac{c}{2a}\right)^2+\left(d-\frac{b^2}{4a^2}-\frac{c^2}{4a^2}\right)=0, \tag{14}$$

from Eq. 14 we can see that the condition for Eq.12 being a circle is:

$$d-\frac{b^2}{4a^2}-\frac{c^2}{4a^2}<0 \tag{15}$$

$$0<4a^2d-b^2-c^2 \tag{16}$$

As the circle equation is overdetermined (namely the a constant), we can impose Eq. 15 as constraint $4a^2d-b^2-c^2=1$. With these considerations

we can reformulate the problem as a Lagrange minimization:

$$\min_{\overline{\mathbf{a}}} ||\underline{\underline{\mathbf{D}}} \cdot \overline{\mathbf{a}}||^2 \qquad \text{s.t.} \qquad \overline{\mathbf{a}}^T \cdot \underline{\underline{\mathbf{C}}} \cdot \overline{\mathbf{a}} = 1 \tag{17}$$

Here, $\underline{\underline{\mathbf{D}}}$ denotes the *design matrix* of size $N \times 4$:

$$\underline{\underline{\mathbf{D}}} = \begin{bmatrix} x_1^2 + y_1^2 & x_1 & y_1 & 1 \\ x_2^2 + y_2^2 & x_2 & y_2 & 1 \\ \vdots & \vdots & \vdots & \vdots \\ x_n^2 + y_n^2 & x_n & y_n & 1 \end{bmatrix}$$

and $\underline{\underline{\mathbf{C}}}$ denotes the *constraint matrix*:

$$\underline{\underline{\mathbf{C}}} = \begin{bmatrix} 0 & 0 & -2 & 0 \\ 0 & 1 & 0 & 0 \\ -2 & 0 & 1 & 0 \\ 0 & 0 & 0 & 0 \end{bmatrix}$$

Following the argumentation of Fitzgibbon et al. (1999), the Lagrange system

can be rewritten as

$$\underline{\underline{\mathbf{S}}} \cdot \overline{\mathbf{a}} = \lambda \underline{\underline{\mathbf{C}}} \cdot \overline{\mathbf{a}} \tag{18}$$

$$\overline{\mathbf{a}}^T \cdot \underline{\underline{\mathbf{C}}} \cdot \overline{\mathbf{a}} = 1 \tag{19}$$

where $\underline{\underline{\mathbf{S}}}$ is the *scatter matrix*, $S = \underline{\underline{\mathbf{D}}}^T \cdot \underline{\underline{\mathbf{D}}}$. This system is readily solved by considering the generalized eigenvectors of (18). If $(\lambda_i, \overline{\mathbf{u}}_i)$ solves (18), then so does $(\lambda_i, \mu\overline{\mathbf{u}}_i)$. Giving

$$\mu_i = \sqrt{\frac{1}{\overline{\mathbf{u}}_i^T \cdot \underline{\underline{\mathbf{C}}} \cdot \overline{\mathbf{u}}_i}} = \sqrt{\frac{1}{\overline{\mathbf{u}}_i^T \cdot \underline{\underline{\mathbf{S}}} \cdot \overline{\mathbf{u}}_i}} \tag{20}$$

and setting $\overline{\mathbf{a}}_i = \mu_i \overline{\mathbf{u}}_i$ solves Eq.19.

The solution of the eigensystem Eq. 18 gives four results. These four results are all local minima of the equation, so selecting the vector which minimizes Eq. 13 yields be the optimal vector.

Verification of the method We will demonstrate the correctness of the algorithm by statistical measurements. We model the beads by two spheres which intersect each other. The contact angle will be the angle measured at the contact ring. This angle can be calculated from geometrical considerations as seen in Fig. 16. We can see that angle α is the complementer angle

of β, whereas β can be calculated from the area of the triangle $O_1O_2P_I$:

$$S = \frac{1}{2} r_1 r_2 \sin\beta \tag{21}$$

$$S = \frac{1}{4}\sqrt{\left(r_1^2 + r_2^2 + d_{O_1,O_2}^2\right)^2 - 2\left(r_1^4 + r_2^4 + d_{O_1,O_2}^4\right)} \tag{22}$$

Here, Eq. 21 is the SAS[8] theorem, while Eq. 22 denotes Heron's formula.

Final formula:

$$\alpha = \pi - \operatorname{asin}\left(\frac{\sqrt{\left(r_1^2 + r_2^2 + d_{O_1,O_2}^2\right)^2 - 2\left(r_1^4 + r_2^4 + d_{O_1,O_2}^4\right)}}{2r_1r_2}\right) \tag{23}$$

gives us the reference angle. In the test we generate two randomly posed intersecting spheres and follow the procedure described above. The measured angles are then averaged and compared with the artificial angle estimation.

Results During the tests we have measured more than 600 pairs of random circles and measured a mean absolute difference of 3.3% compared to the artificial estimations. An example of the interpolated image can be seen in Fig. 17.

The contact angle provides an important information concerning the rate

[8] side-angle-side

of attraction of the particles. While the contact angle can be measured by hand, the automated measurement can provide more consistent and objective information about the chemical forces inside the substrate. An example of the superposed angles can be seen on Fig. 15. In this image, the angle is calculated at several different angles. From these we calculate the average angle. Higher angles correspond to higher attraction forces.

4.3 Nanoparticle transport across phospholipid membrane

For this application, we focus on the interaction of silica nano-particles with large unilamellar liposomes (see Fig. 2 for an image slice example).

While many past studies focused on measuring the end-point nanomaterials and the distribution of their particles, relatively few studies have been dedicated to the understanding of molecular interactions between nanomaterials and cell membrane, which may provide the necessary information to understand how nanomaterials bind and enter cells (Banerji & Hayes, 2007).

Nano-particle transport across cell membrane is important in the development of drug delivery systems, as well as in the question of nano-particle poisoning. We know that hydrophilic nano-particles interact with the lipid membranes. However, if they succeed to enter into the cell and to which

extent, we do not know. Several models have been proposed based from the membrane curvature to even the complete form of the particle.

It was generally believed, that the particles did not enter into mammalian cell by endocytosis[9]. As evidence (Geiser et al., 2005) and (Rothen-Rutishauser et al., 2006) argumented with the entry of ultra fine particles into the red blood cells and cyt-D blocked macrophages[10]. Both of these cells are known for their lack of endocytotic capabilities. However, (Banerji & Hayes, 2007) revealed[11] that in some cases the molecules did not pass through the membranes as expected. This suggests that the nano-particle transport requires an interaction with the membrane. Unlike the nano-particles larger than 30 nm, these 20 nm particles could not "break into" the membrane.

The results of the study (to which this paper has partially contributed) provided in Le Bihan et al. (2009), indicate that silica particles, which are bigger than 30 nm can enter into the liposomes composed of phosphocholine lipid, while smaller particles cannot. This is due to the favourable balance between the adhesion strength and membrane curvature. Smaller particles will not be able to enter because of the less favourable balance.

In this segmentation in addition to the above presented techniques, we

[9]Endocytosis is a process where cells absorb material (such as nanoparticles) from the outside by engulfing (wrapping around) it with their cell membrane.

[10]White blood cells that absorb material foreign to the body (bacteria, etc).

[11]In a study made with gold molecules and a liposomes that mimics the biological membrane.

used a special method for determining the source. Because of the asymmetric shape of the object, a simple constraint bias was not sufficient. We have extracted instead several 2D slices from the image, which we have segmented with the same method, then we have created a complex 3D source from the result. The created source is presented in Fig. 18.

Our segmentation results are summarized in Figures 10, 19, and 20. These show a slice of the input image together with the borders of the segmented objects superimposed in white. We used this evidence to visually check the correctness of the segmentation and the estimation of curvature, which we measured in places of interest (Fig. 21 and Fig. 22).

5 Discussion and conclusion

In this article, we have demonstrated the usefulness of the continuous maximum flow framework for the segmentation of electron nano-tomography images. Despite the presence of noise, lack of contrast and low resolution of images, the method was extended to provide for the interpolation of missing parts of data as well as to cope for the structural noise. Its algorithmic design allows high level of parallelisation which makes it suitable for high resolution images. Moreover, a free implementation exists Couprie (2011), which makes it suitable for research and a useful option for inclusion into

other image processing frameworks.

The method performs reasonably fast in all the above applications.

The method was further improved by adding shape constraints, optimising its performance for the shape-corrupted objects due to the missing wedge effect inherent to the image modality.

The filtering and the segmentation procedure with the maximal flows algorithm and its optimization were applied for two types of nano-material samples.

In the first example, the aim was to find the size of some polystyrene beads and location with respect to a silica bead. The presented method was compared with other classical segmentation methods: thresholding, watershed and graph-cut, and shown to present significantly better performance.

Moreover, we have presented an automatic contact angle measurement algorithm and its statistical evaluation on simulated data. Such automated measurement can provide more consistent and objective information about the chemical forces inside the substrate.

In the second image sample, the max-flow technique was shown to be useful in understanding of molecular interactions between nano-materials and cell membrane, which may provide the necessary information in the understanding of binding and entering of silica nano-particles and large unilamellar liposomes.

As future work, the presented methods will be tested on larger data sets and validated by specialists. In the case of high volume datasets, or many images to segment, the algorithm is implementable on GPU architecture. A GPU implementation would improve the segmentation speed by an order of magnitude.

In the improvement of the algorithm, we also envisage an extension to optimize the flow according to an arbitrary convex-set-function as compared to the simple sphere in the original proposition: Instead of $|\overline{\mathbf{F}}| \leq g$ we could enforce $\overline{\mathbf{F}}(x) \in \Gamma(x)$ where $\Gamma(x)$ is a convex set defined in each point. This would make it possible to optimize the flow for more complex family of curves.

References

Appleton B., Talbot H., (2006), IEEE Transactions on Pattern Analysis and Machine Intelligence, 28, 106

Banerji S., Hayes M., (2007), Langmuir, 23, 3305

Beucher S., Lantuéjoul C., (1979), in Int. Workshop on Image Processing Use of watersheds in contour detection. Rennes, France

Blum H., (1961), in Biological Prototypes and synthetic systems Vol. 1, An associative machine for dealing with the visual field and some of its biological implications. E. E. Bernard and M. R. Kare eds., Plenum Press, New-York, pp 244–260

Boykov Y., Jolly M. P., (2001), ICCV'01, 1, 105

Boykov Y., Kolmogorov V., (2003a), ICCV'03, pp 26–33

Boykov Y., Kolmogorov V., (2003b), in International Conference on Computer Vision Computing geodesics and minimal surfaces via graph cuts. Nice, France, pp 26–33

Breen E., Jones R., (1996), Computer Vision, Graphics and Image Processing, 64, 377

Caselles V., Kimmel R., Sapiro G., (1997a), International Journal on Computer Vision, 22, 61

Caselles V., Kimmel R., Sapiro G., (1997b), International Journal on Computer Vision, 22, 61

Chambolle A., (2004), J. Math. Imaging Vis., 20, 89

Chan W. C., (2006), Biology of Blood and Marrow Transplantation, 12, 87

Chen H., Hughes D. D., Chan T.-A., Sedat J. W., Agard D. A., (1996), Journal of Structural Biology, 116, 56

Cheng P., Li D., Boruvka L., Rotenberg Y., Neumann A., (1990), Colloids and Surfaces, 43, 151

Couprie M., , 2011, Pink image processing library, http://www.esiee.fr/~coupriem/pink.tgz, ESIEE, Paris

Downing K. H., Sui H., Auer M., (2007), Analytical Chemistry, 79, 7949

Fendler J., (1998), Nanoparticles and nanostructured films. Wiley-VCH Weinheim

Fisker R., Carstensen J., Hansen M., Bodker F., Morup S., (2000), Journal of Nanoparticle Research, 2, 267

Fitzgibbon A., Pilu M., Fisher R. B., (1999), IEEE Transactions on Pattern Analysis and Machine Intelligence, 21, 476

Ford J. L. R., Fulkerson D. R., (1962), Flows in Networks. Princeton University Press, Princeton, NJ

Ford L. R., Fulkerson D. R., (1956), Canadian Journal of Mathematics, 8, 399

Foundation F. S., , 2010, The GNU Scientific Library (GSL)

Geiser M., Rothen-Rutishauser B., Kapp N., Schürch S., Kreyling W., Schulz H., Semmler M., Im Hof V., Heyder J., Gehr Environ P., (2005), Environ Health Perspect., pp 1555–1560

Goldman R., (2005), Comput. Aided Geom. Des., 22, 632

Grady L., (2010), tpami, 32, 321

Hoppe W., (1974), Naturwissenschaften, 61, 239

Hough P., , 1962, Methods and means for recognizing complex patterns, US Patent 3069654

Illingworth J., Kittler J., (1988), Comput. Vision Graph. Image Process., 44, 87

Kak A. C., Slaney M., (1999), Principles of Computerized Tomographic Imaging. IEEE Press

Kang Y., Engelke K., Kalender W. A., (2004), Medical Image Analysis, 8, 35

Kass M., Witkin A., Terzopoulos D., (1988a), IJCV, 1, 321

Kass M., Witkin A., Terzopoulos D., (1988b), International Journal of Computer Vision, 1, 321

Kolmogorov V., Zabin R., (2004), PAMI, 26, 147

Le Bihan O., Bonnafous P., Marak L., Bickel T., Trépout S., Mornet S., De Haas F., Talbot H., Taveau J., Lambert O., (2009), Journal of structural biology

Lobregt S., Verbeek P., Groen F., (1980), IEEE Transactions on Pattern Analysis and Machine Intelligence, 2, 75

Martin D., Fowlkes C., Tal D., Malik J., (2001), iccv, 2, 416

Mastronarde D. N., (1997), Journal of Structural Biology, 120, 343

Meyer F., Beucher S., (1990), Journal of Visual Communication and Image Representation, 1, 21

Midgley P., Ward E., Hungría A., Thomas J., (2007), Chem Soc Rev, 36, 1477

Möebus G., Inkson B., (2003), Microscopy and Microanalysis, 9, 176

Nel A., Xia T., Madler L., Li N., (2006), Science, 311, 622

Nickell S., Fôrster F., Linaroudis A., Net W. D., Beck F., Hegerl R., Baumeister W., Plitzko J. M., (2005), Journal of Structural Biology, 149, 227

Nikolova M., Esedoglu S., Chan T. F., (2006), SIAM JAM, 66, 1632

Paragios N., (2000), PhD thesis, INRIA Sophia Antipolis

Rosi N., Mirkin C., (2005), Chem. Rev, 105, 1547

Rothen-Rutishauser B. M., Schurch S., Haenni B., Kapp N., Gehr P., (2006), Environ. Sci. Technol, 40, 4353

Schmid G., (2004), Nanoparticles: from theory to application. Wiley-VCH

Senan S., van Sornsen de Koste J., Samson M., Tankink H., Jansen P., Nowak P. J. C. M., Krol A. D. G., Schmitz P., Lagerwaard F. J., (1999), Radiotherapy and Oncology, 53, 247

Sethian J., (1999a), Level set methods and fast marching methods. Cambridge University Press

Sethian J. A., (1999b), Level Set Methods and Fast Marching Methods. Cambridge University Press

Strang G., (1983a), Mathematical Programming, 26, 123

Strang G., (1983b), Math. Prog., pp 123–143

Taveau J., Nguyen D., Perro A., Ravaine S., Duguet E., Lambert O., (2008), Soft Matter, 4, 311

Valden M., Lai X., Goodman D. W., (1998), Science, 281, 1647

Woehrle G., Hutchison J., Ozkar S., Finke R., (2006), Turkish Journal of Chemistry, 30, 1

Zrour R., Couprie M., (2005), in Andres E., Damiand G. Lienhardt P., eds, Discrete Geometry for Computer Imagery: 12th International Conference, DGCI 2005 Vol. 3429 of LNCS, Discrete bisector function and euclidean skeleton. Springer, Poitiers, France, pp 216–227

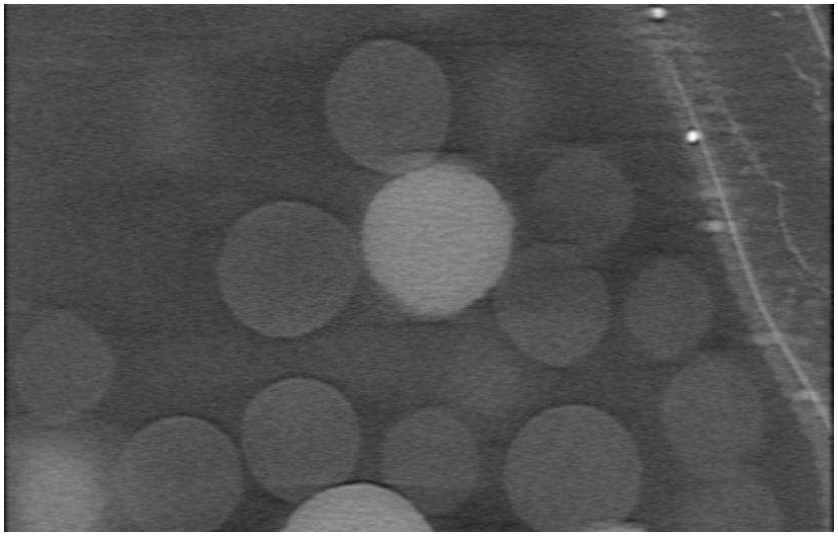

Figure 1: An original TEM image slice on the polystyrene beads nucleated around a silica one.

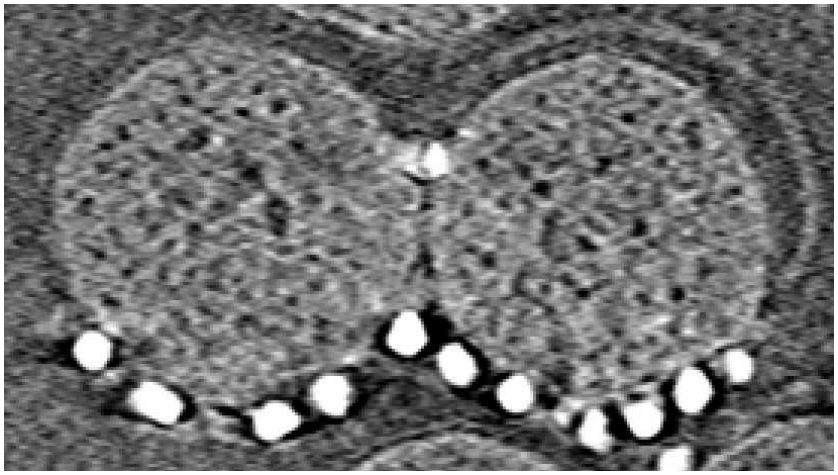

Figure 2: An original image slice of silica nano particles with large unilamellar liposomes.

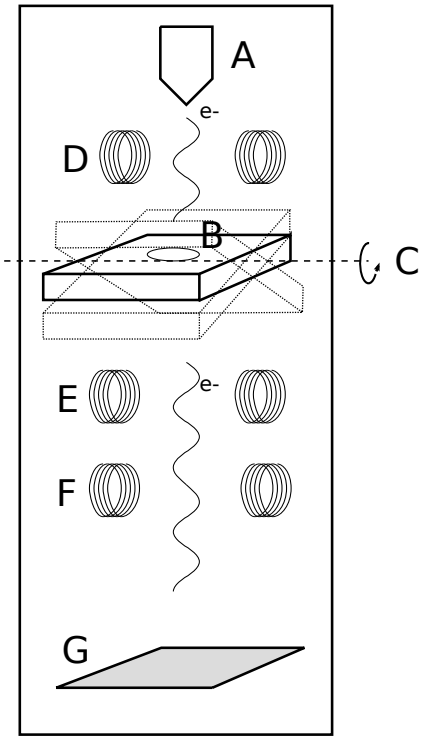

Figure 3: Simplified schematics of a transmission electron microscope for nano-tomography. A: electron source, B: Sample, C: Tiltable stage, D: Condenser magnetic lens, E: Diffraction lens, F: Projection lens, G: Sensor, .

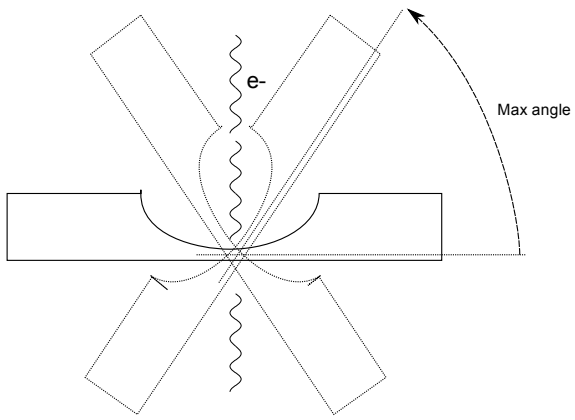

Figure 4: As the sample is thin in one direction only, it is not possible to rotate it fully around the electron beam. The maximum tilt angle is usually around 70° or so.

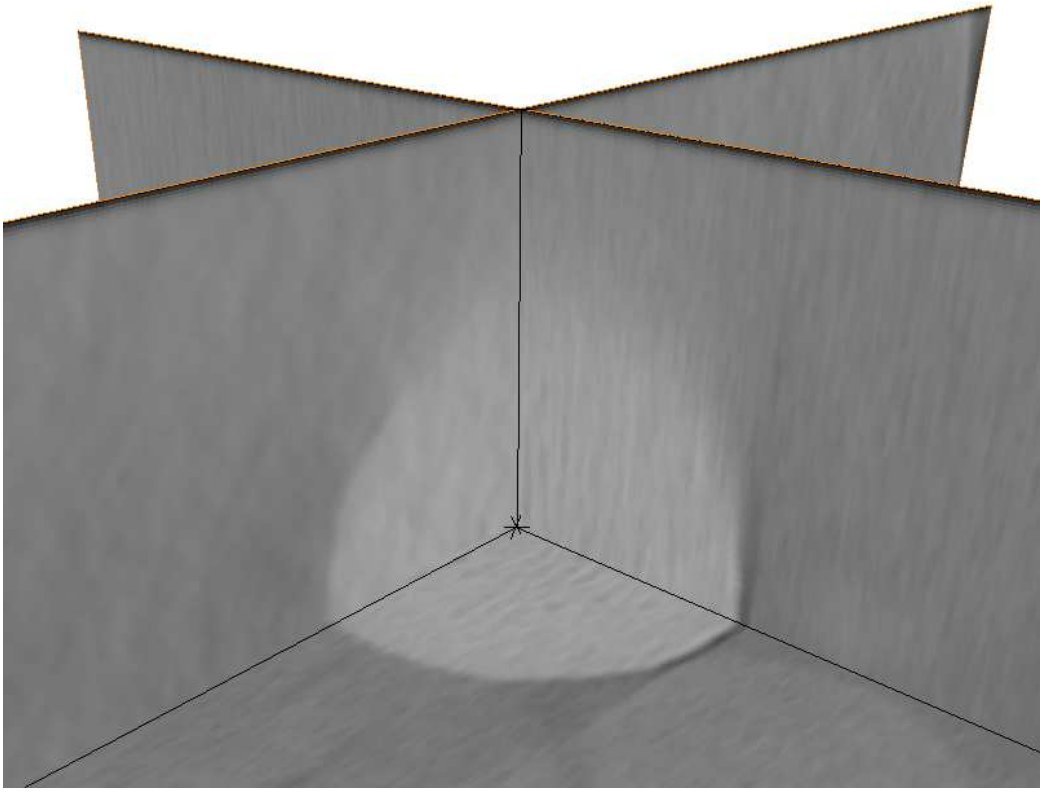

Figure 5: This image represents some artifacts of the missing wedge effect commonly observed in electron nanotomography. Because it is not possible to rotate the sample fully around the beam, edges perpendicular to the main beam direction are weak and elongated due to missing wedge effect, and the image is very noisy.

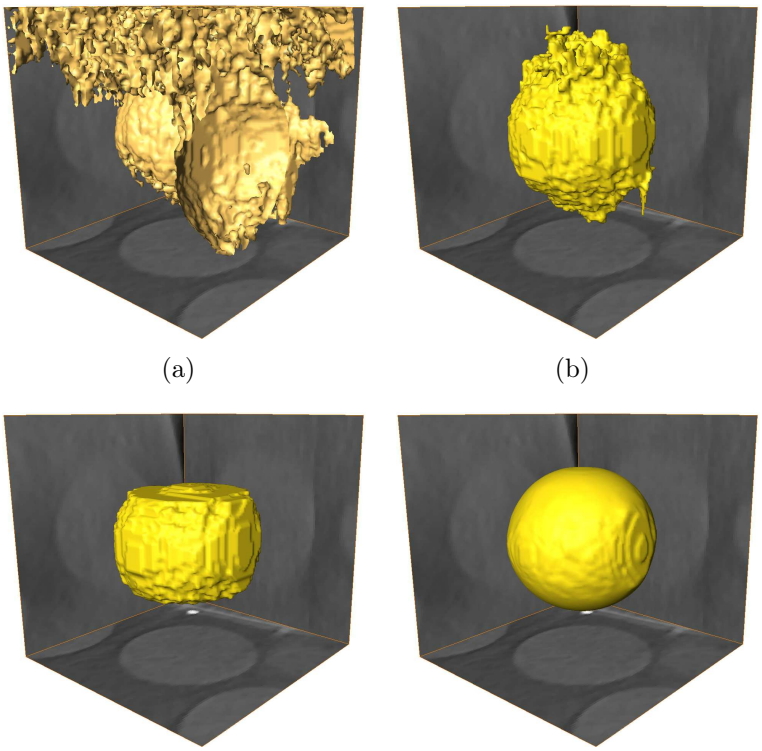

Figure 6: Application of various 3D segmentation methods on nanotomography images. (a) Optimal threshold ; (b) Watershed ; (c) Graph cuts ; (d) Continuous maximum flows. Only this last method provides a good result in our case.

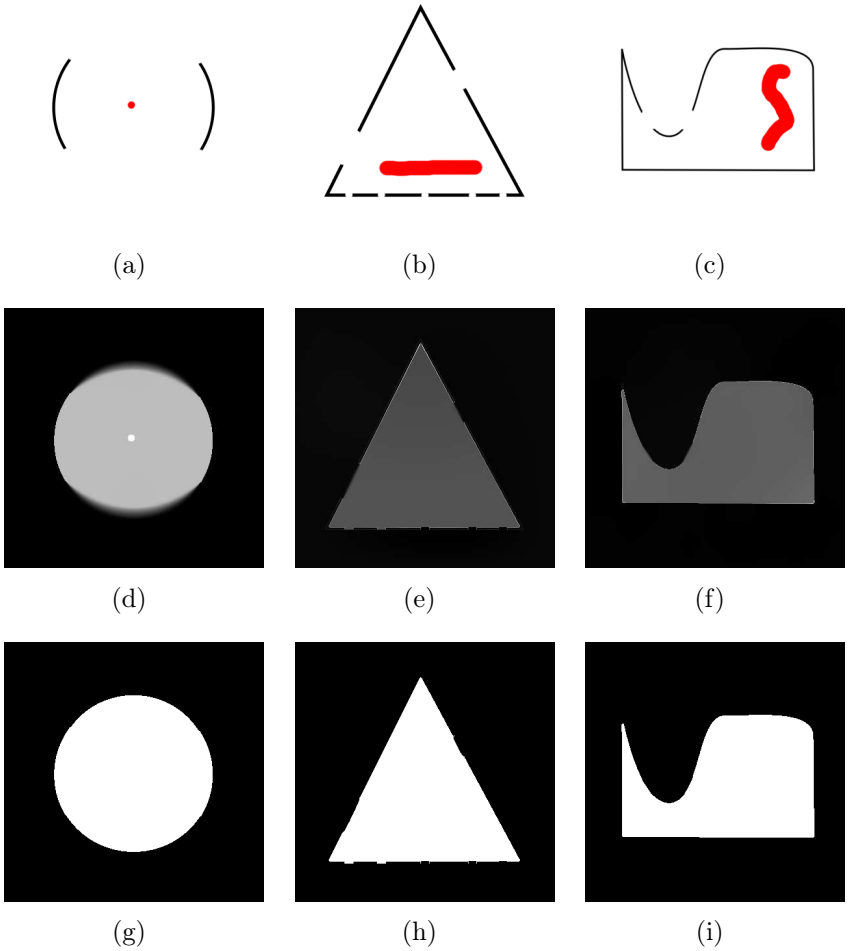

Figure 7: Examples of continuous maximum flow segmentation. The sources are marked in red. The sinks are the border of the images. In the image (a), the constraint-field is affected with a circular bias, whereas the images (b) and (c) are not altered. We can see, that the segmentation succeeds even on incomplete or concave objects. Images (d), (e) and (f) represent the partially converged pressure fields, while images (g), (h) and (i) are the final segmentations.

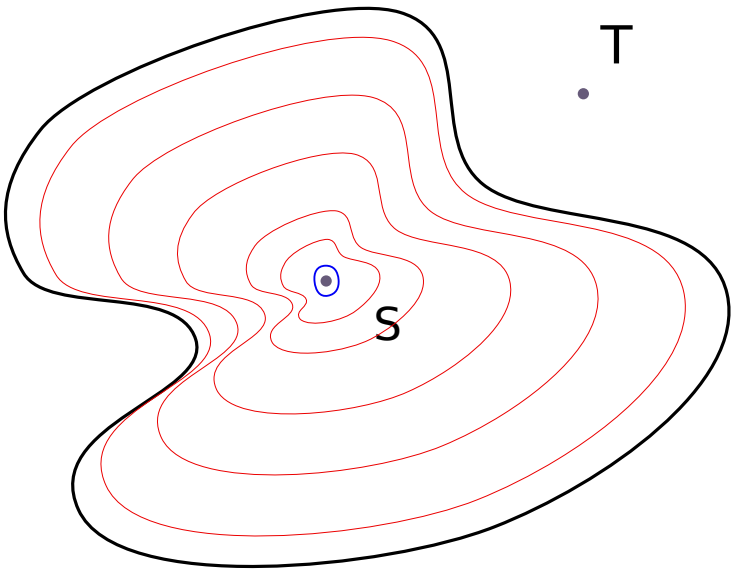

Figure 8: We assume that our image is constant 1 everywhere except on the black curve, where its value is small (ε). Now if we consider the integral on the black curve, than this integral will also be small. We specify pointwise source and sink S and T respectively. We would like to find the optimum curve, however as we take curves towards the source (the red curves), the integral tends to zero. A small curve around the source (blue) will have smaller integral than the black curve.

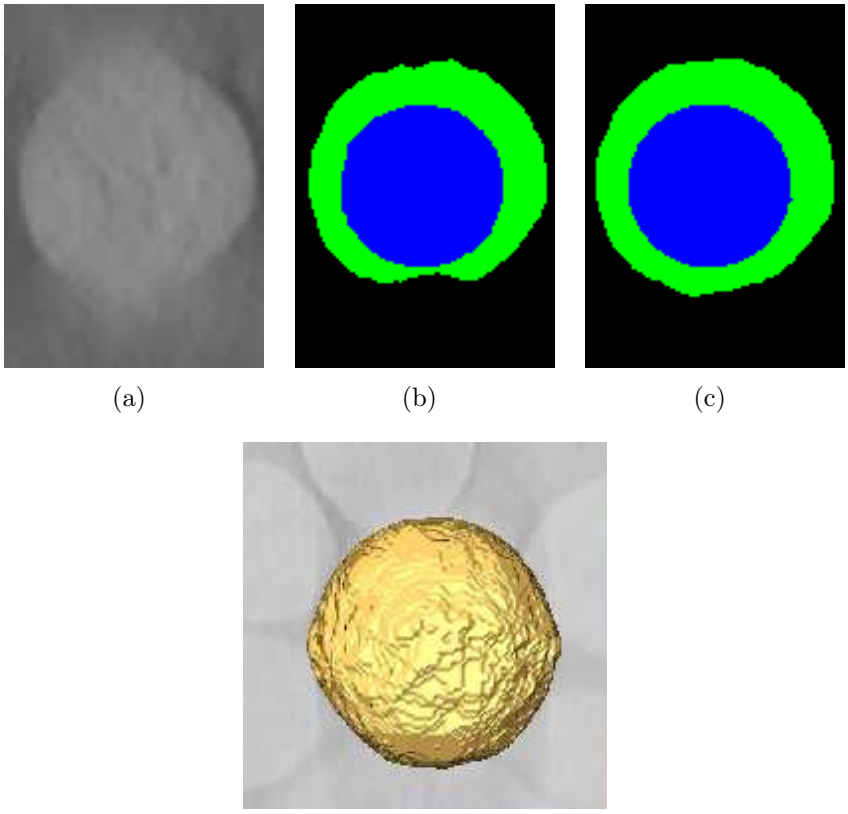

Figure 9: Slice of a segmented ball with the maximum flows method. (a) Original data. (b) Unweighted cost function segmentation result in green (in blue - marker). (c) Weighted cost function result (same color coding as in (b)). (d) 3D segmentation result.

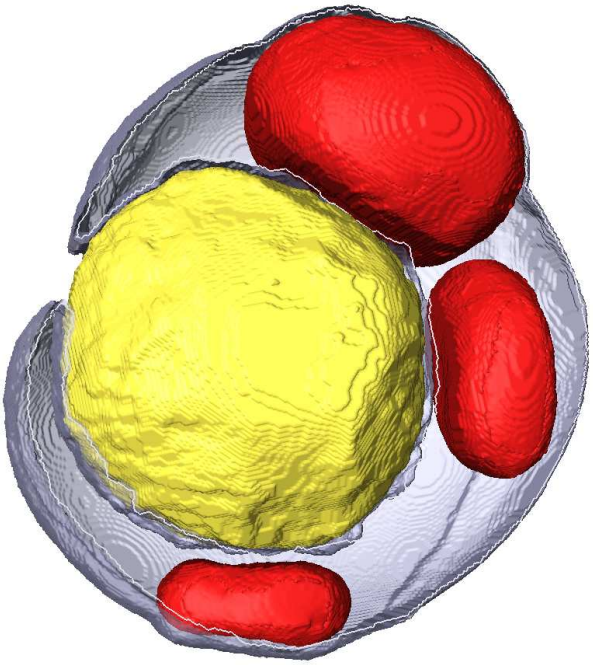

Figure 10: Nanoparticle entering into the cell. The membrane has been cut in half for better visibility.

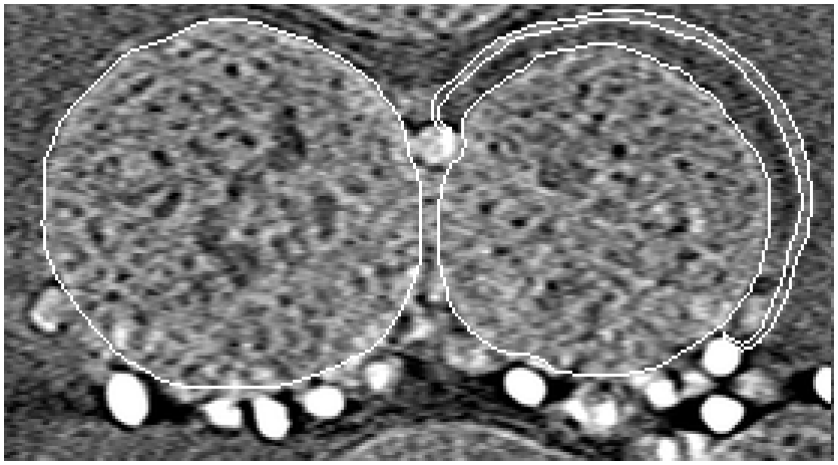

Figure 11: Summary of segmentation procedure results: segmentation accuracy of nanoparticle, membrane and radii of curvature. Results superimposed in white over the original image data.

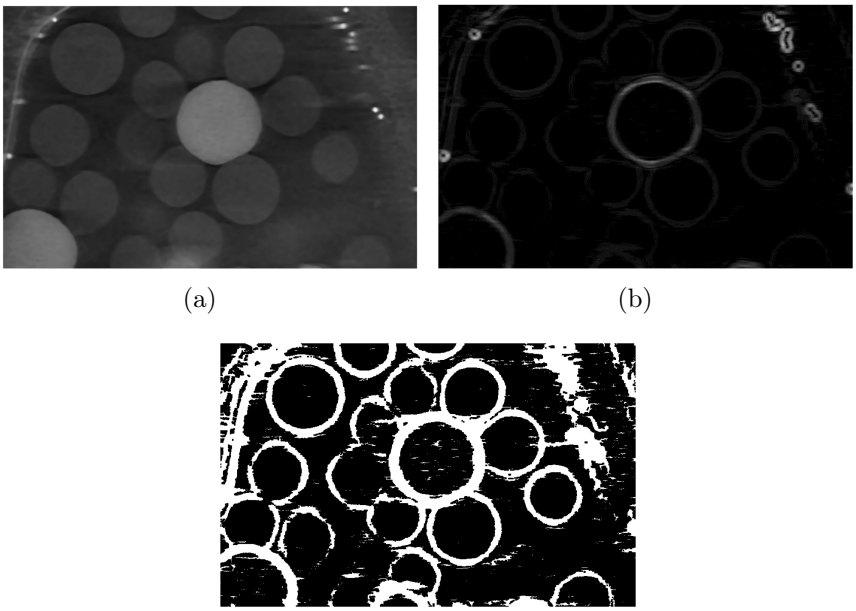

(a) (b)

(c)

Figure 12: The pre-processing steps: (a) Median filter. (b) First derivatives. (c) Morphological opening and closing results.

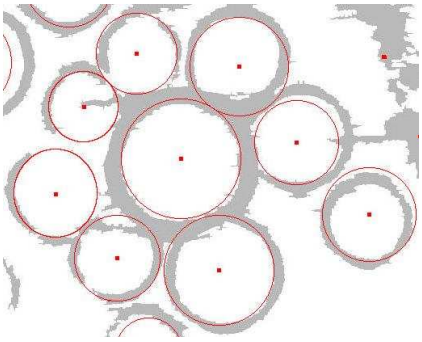

Figure 13: A pre-processed image slice together with the Hough circle transform result.

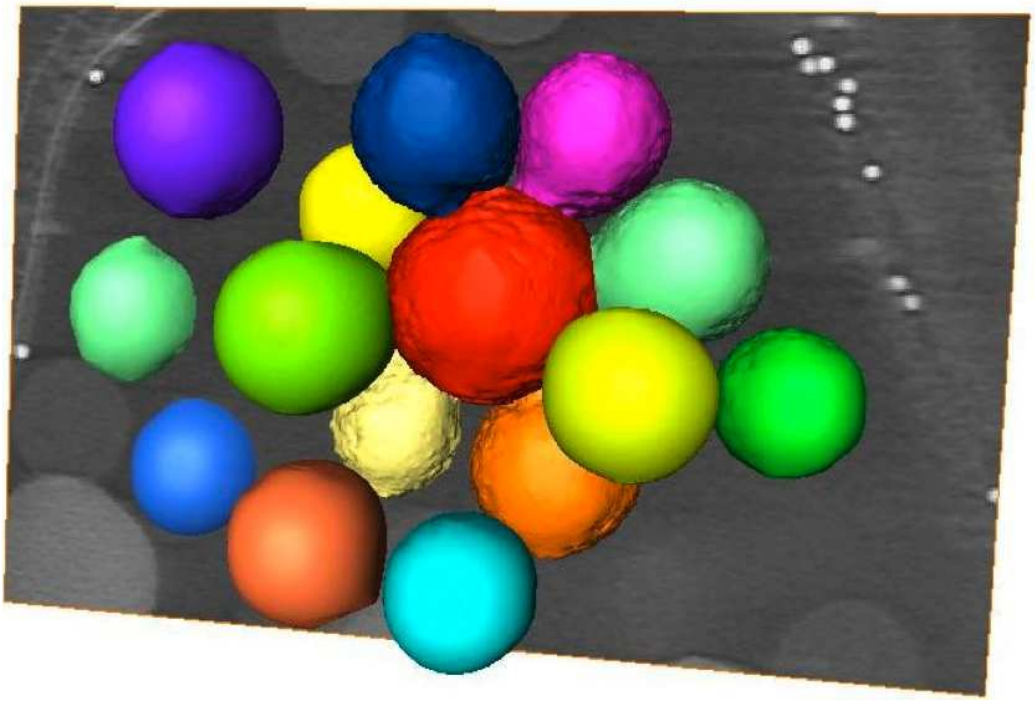

Figure 14: Polystyrene and silica beads embedded in a substrate. The coloration is arbitrary.

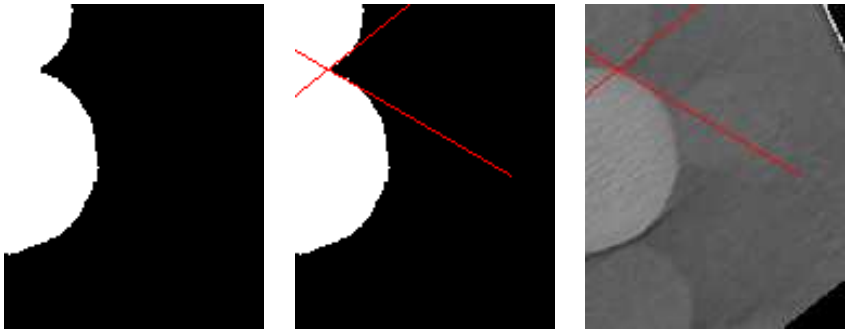

(a) (b) (c)

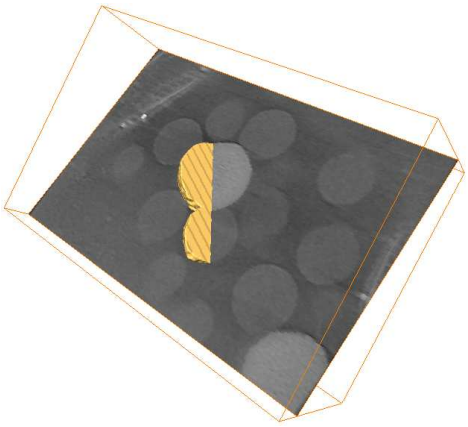

(d)

Figure 15: Contact angle measurement. The segmented object (a), the estimated angle (b), the angle superimposed to the object (c) and the cut plane in the 3D image (d)

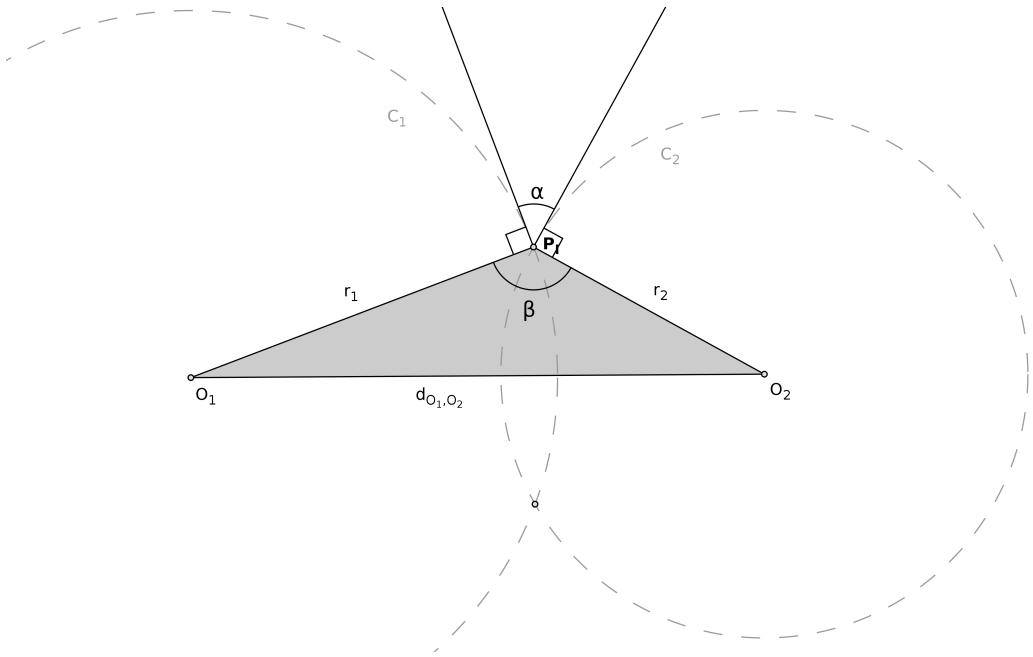

Figure 16: Contact angle measurement of two artificial spheres

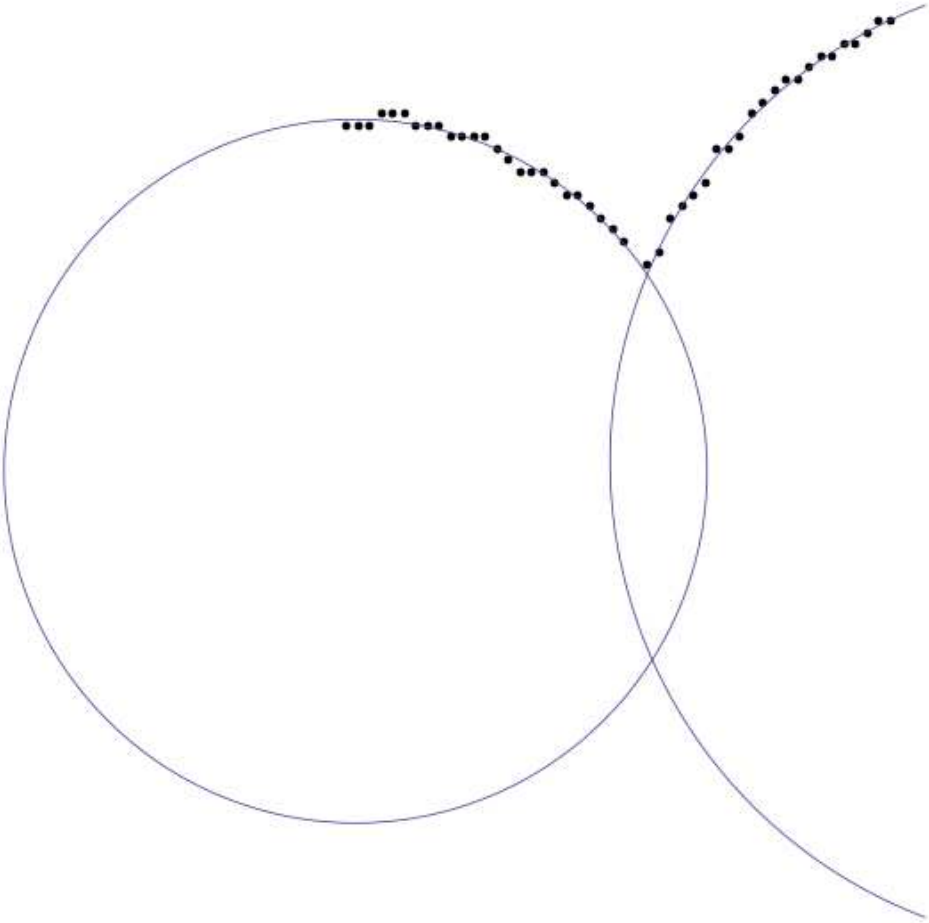

Figure 17: Circe fitting on two arcs

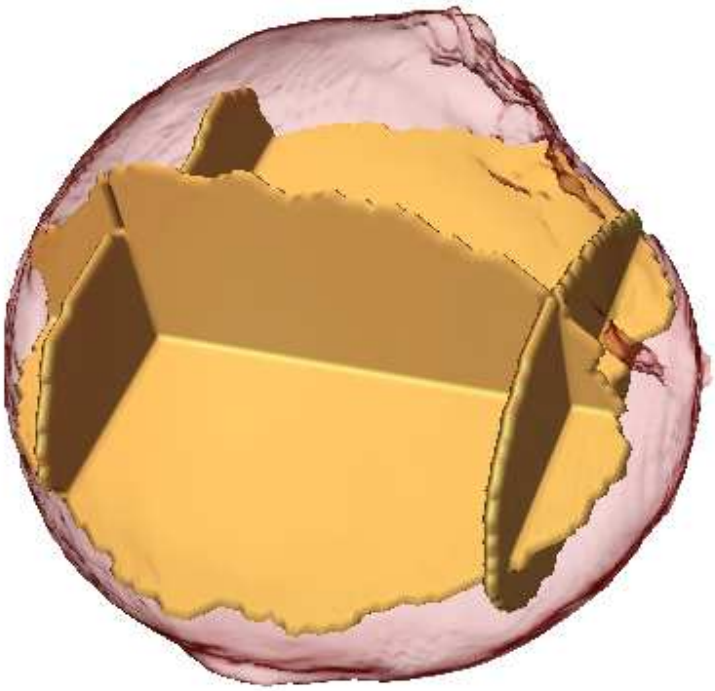

Figure 18: The inner yellow object is the source that have been generated by segmenting the 2D slices with good visibility.

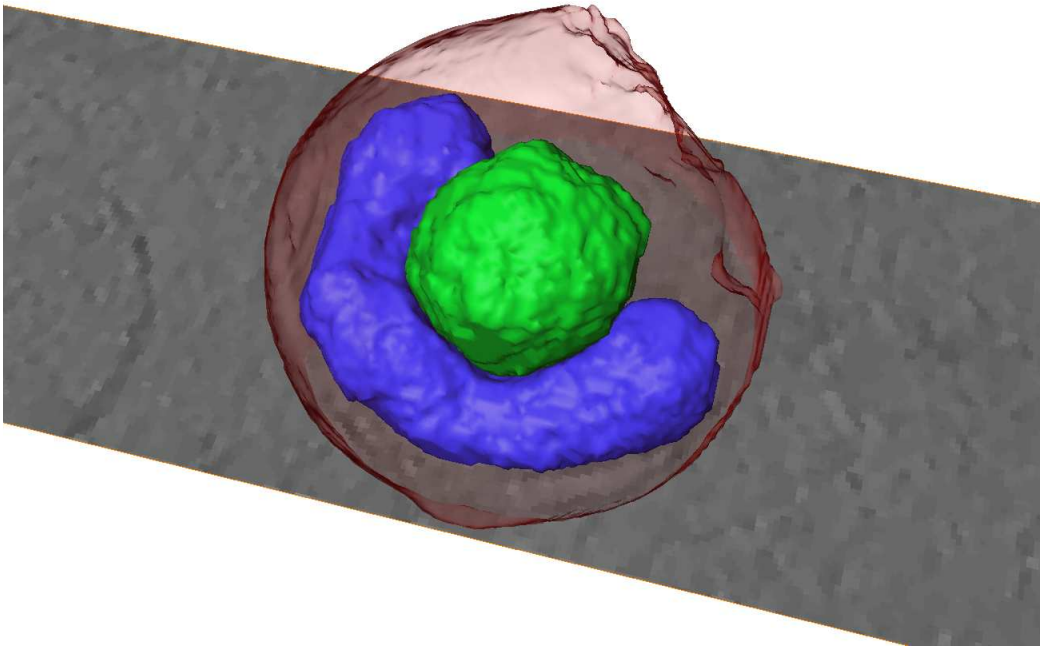

Figure 19: Nanoparticle penetrated into the cell. The inner membrane wraps around the particle.

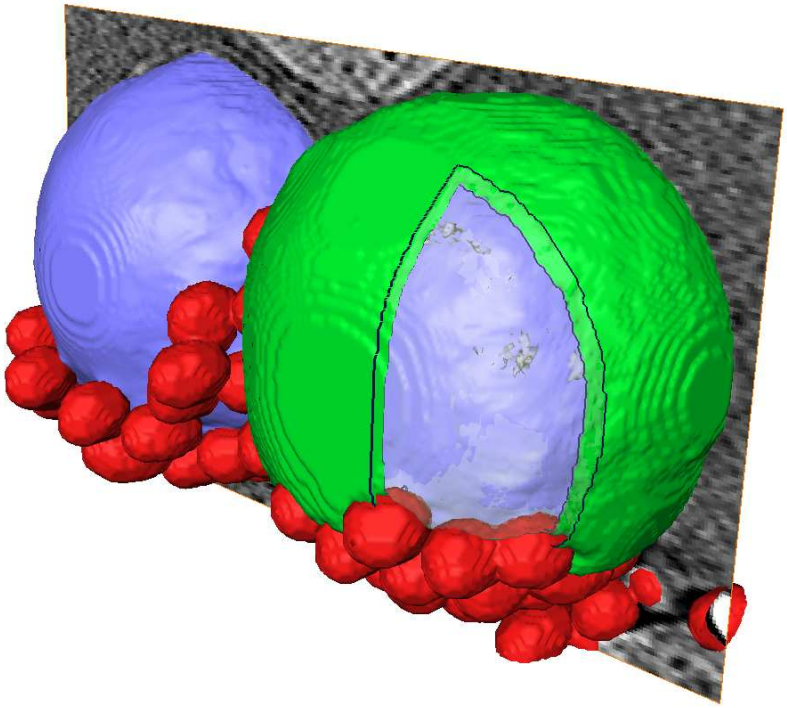

Figure 20: Interaction of the lipidic membrane with the nanoparticle. The red pieces are the gold markers that were used for the reconstruction.

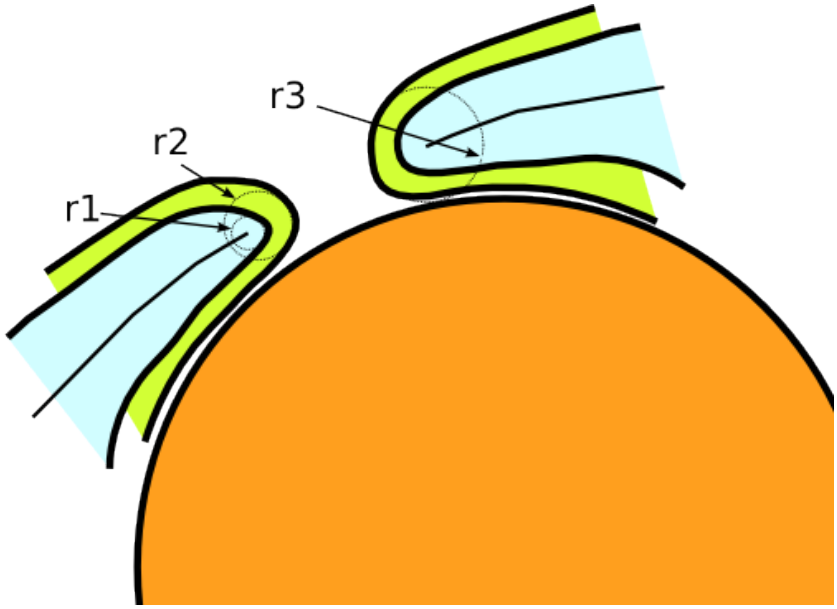

Figure 21: Curvature estimation. R1 is the radius of the inner maximal ball, R1 the radius of the external maximal ball and R3 the radius to the nano-particle. Depending on the configuration either R2 or R3 yield a robust curvature estimation.

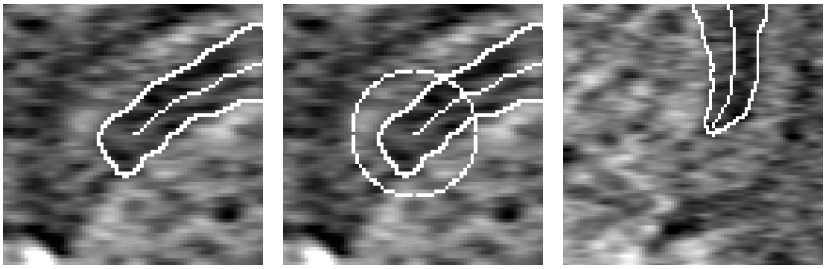

(a) (b) (c)

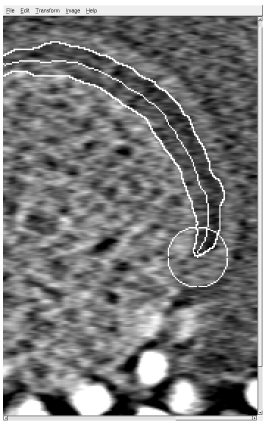

(d)

Figure 22: The estimated curvatures.